



Publication Year	2016
Acceptance in OA@INAF	2020-07-03T10:13:40Z
Title	CONSTRAINING POLARIZED FOREGROUNDS FOR EoR EXPERIMENTS. I. 2D POWER SPECTRA FROM THE PAPER-32 IMAGING ARRAY
Authors	Kohn, S. A.; Aguirre, J. E.; Nunhokee, C. D.; BERNARDI, GIANNI; Pober, J. C.; et al.
DOI	10.3847/0004-637X/823/2/88
Handle	http://hdl.handle.net/20.500.12386/26313
Journal	THE ASTROPHYSICAL JOURNAL
Number	823



CONSTRAINING POLARIZED FOREGROUNDS FOR EoR EXPERIMENTS. I. 2D POWER SPECTRA FROM THE PAPER-32 IMAGING ARRAY

S. A. KOHN¹, J. E. AGUIRRE¹, C. D. NUNHOKEE², G. BERNARDI^{2,3,4}, J. C. POBER⁵, Z. S. ALI⁶, R. F. BRADLEY^{7,8,9}, C. L. CARILLI^{10,11},
D. R. DEBOER⁶, N. E. GUGLIUCCI¹², D. C. JACOBS¹³, P. KLIMA⁸, D. H. E. MACMAHON¹⁴, J. R. MANLEY³, D. F. MOORE¹,
A. R. PARSONS^{6,14}, I. I. STEFAN¹¹, AND W. P. WALBRUGH³

¹ Department of Physics and Astronomy, University of Pennsylvania, Philadelphia, PA, USA; saulkohn@sas.upenn.edu

² Department of Physics and Electronics, Rhodes University, Grahamstown, South Africa

³ SKA South Africa, Pinelands, South Africa

⁴ Harvard-Smithsonian Center for Astrophysics, Cambridge, MA, USA

⁵ Department of Physics, Brown University, Providence, RI, USA

⁶ Astronomy Department, University of California, Berkeley, CA, USA

⁷ Department of Electrical and Computer Engineering, University of Virginia, Charlottesville, VA, USA

⁸ National Radio Astronomy Observatory, Charlottesville, VA, USA

⁹ Department of Astronomy, University of Virginia, Charlottesville, VA, USA

¹⁰ National Radio Astronomy Observatory, Socorro, NM, USA

¹¹ Cavendish Laboratory, Cambridge, UK

¹² Saint Anselm College, Manchester, NH, USA

¹³ School of Earth and Space Exploration, Arizona State University, Tempe, AZ, USA

¹⁴ Radio Astronomy Laboratory, University of California, Berkeley, CA, USA

Received 2016 February 8; accepted 2016 March 29; published 2016 May 25

ABSTRACT

Current generation low-frequency interferometers constructed with the objective of detecting the high-redshift 21 cm background aim to generate power spectra of the brightness temperature contrast of neutral hydrogen in primordial intergalactic medium. Two-dimensional (2D) power spectra (power in Fourier modes parallel and perpendicular to the line of sight) that formed from interferometric visibilities have been shown to delineate a boundary between spectrally smooth foregrounds (known as the *wedge*) and spectrally structured 21 cm background emission (the *EoR window*). However, polarized foregrounds are known to possess spectral structure due to Faraday rotation, which can leak into the EoR window. In this work we create and analyze 2D power spectra from the PAPER-32 imaging array in Stokes I, Q, U, and V. These allow us to observe and diagnose systematic effects in our calibration at high signal-to-noise within the Fourier space most relevant to EoR experiments. We observe well-defined windows in the Stokes visibilities, with Stokes Q, U, and V power spectra sharing a similar wedge shape to that seen in Stokes I. With modest polarization calibration, we see no evidence that polarization calibration errors move power outside the wedge in any Stokes visibility to the noise levels attained. Deeper integrations will be required to confirm that this behavior persists to the depth required for EoR detection.

Key words: cosmology: observations – dark ages, reionization, first stars – polarization – techniques: interferometric

1. INTRODUCTION

The Epoch of Reionization (EoR) marks an era in which the intergalactic medium (IGM) underwent a phase transition from neutral to ionized. Between redshifts $\sim 8 < z < 200$, the first stars and black holes formed from clouds of hydrogen left over from recombination and could, for the first time since the last-scattering surface, ionize neutral hydrogen. Due to the huge range in redshift (i.e., volume) over which this process occurs, the ability to intensity map neutral hydrogen via its 21 cm (≈ 1420 MHz) hyperfine transition over cosmic time (i.e., different redshifted frequencies) as been recognized as one of the most powerful probes of cosmic dawn (e.g., Furlanetto et al. 2006).

Many experiments seek to constrain the power spectra of 21 cm brightness across different redshifts using low-frequency interferometers. These instruments include the GMRT (Paciga et al. 2011), LOFAR¹⁵ (van Haarlem et al. 2013), the MWA¹⁶ (Tingay et al. 2013), and the Precision Array for Probing the

Epoch of Reionization; PAPER¹⁷ (Parsons et al. 2010). To date, PAPER has imposed the strongest limits on the 21 cm power spectrum at $z = 7.7$, 8.4 and 10.3, respectively (Parsons et al. 2014; Ali et al. 2015; Jacobs et al. 2015; Moore et al. 2016).

The biggest challenge shared by all of these experiments is the overwhelming power of foreground emission, orders of magnitude brighter than the reionization signal (e.g., Bernardi et al. 2009; Pober et al. 2013; Dillon et al. 2014). Foreground emission, however, is expected to be intrinsically spectrally smooth over tens of MHz, whereas the inherent cloudiness of neutral hydrogen before and during reionization is expected to vary over a few MHz scales. This different spectral behavior still constitutes the most powerful leverage to separate the two signals. Looking at their footprint in power spectrum space, foregrounds are expected to be confined into a “wedge”-shaped region, leaving an open *EoR window* for interferometric reionization studies to take advantage of (e.g., Datta et al. 2010; Morales et al. 2012; Thyagarajan et al. 2013; Trott et al. 2012; Pober et al. 2013, 2014; Liu et al. 2014a, 2014b; Dillon et al. 2015a, 2015b; Thyagarajan et al. 2015b, 2015a). PAPER EoR observations implement foreground avoidance

¹⁵ www.lofar.org

¹⁶ www.mwatelescope.org

¹⁷ eor.berkeley.edu

strategies, filtering away the wedge. However, by combining knowledge of the wedge with foreground removal (modeling and subtracting sources from the data), significantly more EoR signal could be recovered, especially if foreground spectra deviate from perfect smoothness (Chapman et al. 2016).

Polarized synchrotron emission from our own Galaxy and from extragalactic radio sources is not expected to be confined within the “wedge”-shaped region due to spectral structure from Faraday rotation, and imperfect calibration may leak Faraday rotated polarized emission to such emission into the total intensity, representing a potentially serious contamination to the EoR signal (Bernardi et al. 2010; Jelić et al. 2010; Moore et al. 2013). Recent observations in the 100–200 MHz band, covering selected sky areas have revealed that Galactic diffuse polarized synchrotron radiation seems to be ubiquitous (Bernardi et al. 2009, 2010; Jelić et al. 2014) with peak emission up to 15 K (Jelić et al. 2015), but find a dearth of polarized point sources. A study of the depolarization of point sources by Farnes et al. (2014) showed a systematic trend for depolarization of steep-spectrum point sources as frequency decreased, resulting in very low polarization fractions ($<<1\%$) below 300 MHz. Bernardi et al. (2013) surveyed the largest sky area in polarization to date, showing that polarized extragalactic sources are significantly depolarized with respect to higher frequencies, detecting only one source with polarization fraction greater than 2% over $\sim 2400^\circ$. This low level of intrinsic polarization appears to be corroborated by recent results from LOFAR (Asad et al. 2015). Bernardi et al. (2013) further showed that diffuse polarized emission largely occurs at rotation measure (RM) values $<|10 - 15| \text{ rad m}^{-2}$ that are expected to contaminate k -modes up to $k \sim 0.05 \text{ Mpc}^{-1}$ at $z = 8$ (Moore et al. 2013).

As PAPER and other instruments are beginning to reach levels of sensitivity comparable with the expected reionization signal (e.g., Lidz et al. 2008), polarized leakage may become a dominant systematic. For PAPER, the effective polarization leakage over its long season averages has been limited to be below the current upper limits on the 21 cm power spectrum at the relevant k -modes (Moore et al. 2016). Asad et al. (2015) found evidence of very small amounts of polarized leakage (0.2%–0.3%) into an EoR window constructed from the central 4° of the LOFAR 3C196 field.

As the PAPER collaboration looks forward to analyzing data from the instrument’s final configuration with 128 dual-polarization dipole antennae in a highly redundant array configuration, and as the Hydrogen Epoch of Reionization Array (HERA)¹⁸ is now under construction (see, e.g., Ewall-Wice et al. 2016; Neben et al. 2016), this level of leakage may become perceivable in the power spectra measured by these instruments.

It is therefore timely to constrain both instrumental and astrophysical polarization to allow instruments such as PAPER and HERA to make the best possible measurements of the 21 cm power spectrum. In this paper we aim to constrain the polarized foreground footprint in the two-dimensional (2D) power spectrum and its correlation with the total intensity wedge shape, and quantify the effects of calibration within the wedge for all four Stokes parameters.

This work is the first in a series of papers that will study the impact polarization leakage for the PAPER and HERA

experiments. This paper details how 2D polarized power spectra created from visibilities using the delay transform with basic direction-independent calibration can be used to diagnose instrument systematics.

The layout of this paper is as follows. In Section 2 we provide a brief description of the PAPER array in its imaging configuration, the data from which this paper is based, and describe its calibration and reduction. We also describe the method used to create 2D power spectra in this section. We analyze the power spectra in Section 3 and discuss the implications of our findings and conclude in Section 4.

2. OBSERVATIONS

The PAPER 32-antenna array relied on its highly redundant configuration in order to take the measurements resulting in the strong upper limits on the 21 cm power spectrum (Parsons et al. 2014; Jacobs et al. 2015; Moore et al. 2016). However, for three nights in 2011 September, the 32 elements were reconfigured into an polarized imaging configuration. We present measurements taken overnight on 2011 September 14–15 over local sidereal times (LSTs) 0–5 hr.

2.1. Observation and Reduction

Antennae were arranged in a pseudo-random scatter within a 300 m diameter circle, the layout of which is shown in Figure 1. This allowed us to obtain resolutions between $15'$ and $25'$ across the bandwidth (100–200 MHz nominally, although in reality this extends 110–185 MHz due to band edge effects and VHF TV). Drift-scan visibilities were measured every 10.7 s, and divided into data sets about 10 minutes in length. We express an interferometric visibility V_{ij}^{pq} between antennae i (with dipole arm p , which can be x (east–west) or y (north–south) for PAPER dipoles) and j (with dipole arm q), in directional cosines l and m for frequency ν at time t , as:

$$V_{ij}^{pq}(\nu, t) = g_i^p g_j^{q*} \exp(-2\pi i \nu \tau_{pq}) \times \int d\Omega A^{pq}(\Omega, \nu) S(\Omega, \nu) \exp\left(\frac{-i\nu}{c} \mathbf{b}(t) \cdot \hat{\mathbf{s}}(\Omega)\right) \quad (1)$$

where the g terms represent the complex gains for each antenna and dipole arm, A^{pq} is the polarized beam, and S is the sky. The product $\mathbf{b}(t) \cdot \hat{\mathbf{s}}(\Omega)$ represents the projection of the baseline between i and j with respect to an arbitrary location on the sky. The motivation for including the term for the delay between dipole arms p and q , τ_{pq} , is given in Section 2.2.3. This delay is clearly zero if $p = q$.

Visibilities were obtained from correlating both x and y dipoles, forming V^{xx} , V^{xy} , V^{yx} , and V^{yy} . Frequencies from 100 to 200 MHz were sampled into 2048 channels. Data were delay-filtered to 203 frequency channels (see the appendix of Parsons et al. 2014). Cross-talk was modeled and removed by subtracting the average power over the 5 hr of observation, which extended across LST = 0–5 hr. An initial RFI-flagging removed any outliers more than 6σ from a spectrally smooth profile.

2.2. Calibration

Calibration took place in three stages detailed below: a first-order delay-space calibration for the initial gains and phases with respect to Pictor A; an absolute calibration using imaging

¹⁸ www.reionization.org

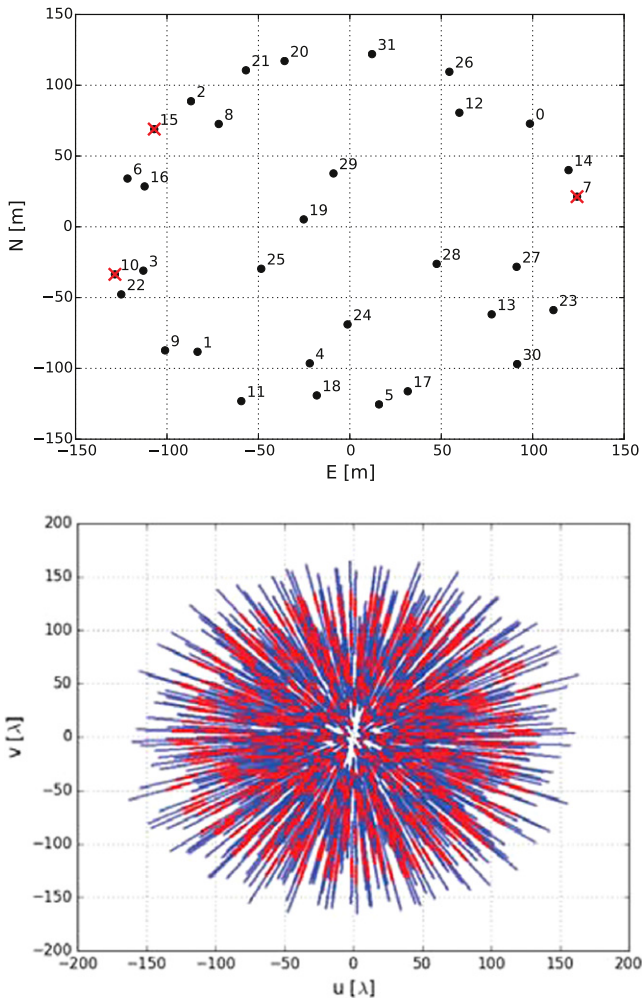


Figure 1. PAPER-32, dual-pol antenna imaging configuration (top). They were arranged in a pseudo-random scatter within a ~ 300 m diameter circle to maximize instantaneous uv coverage (bottom). uv coverage is shown for 100–200 MHz over 203 channels in blue and for 146–166 MHz over 20 channels in red (the latter being the frequencies used in our power spectrum analysis). Malfunctioning antennae identified during calibration are overlaid with red crosses (and are excluded from the uv coverage map).

with respect to Pictor A and Fornax A; and a polarimetric correction for the τ_{xy} phase term in the V^{xy} and V^{yx} visibilities. Traditional polarimetric calibration proceeds by observing a source with a known polarization angle and solving for up to seven direction-independent terms in the Jones matrix (e.g., Thompson et al. 1986; Hamaker et al. 1996) as well as correcting for the effects of the primary beam. As discussed in Section 1, given the dearth of suitable calibrators at our observing frequencies, especially at the relatively low resolution and sensitivity of the array, we proceeded with polarized calibration using different techniques as described in Section 2.2.3 below.

2.2.1. Initial Calibration

A first-order gain and phase calibration was performed by a similar approach to Jacobs et al. (2013). Each 10-minute drift scan data set was phased to the known position of Pictor A using AIPY¹⁹ routines.

The gain term in Equation (1) was approximated as

$$g_i^p = G_i^p \exp(-2\pi i \nu \tau_{ip}) \quad (2)$$

and the required delay τ_{ip} offset of the uncalibrated delay tracks to the real position on the sky solved for to obtain a phase calibration; the absolute flux calibration G_i^p was found by isolating the tracks of Pictor A in delay space and applying the required flux scale across the band (for a discussion of delay-space calibration see Parsons et al. 2012b, and Figure 4).

2.2.2. Absolute Calibration

Visibilities were converted to CASA²⁰ Measurement Sets to be further calibrated using a custom pipeline developed around CASA libraries. Snapshot images were generated for each 10-minute observation by Fourier transforming the visibilities. We used uniform weights and the multi-frequency synthesis algorithm to further improve the uv coverage. Dirty images were deconvolved down to a 5 Jy threshold using the Cotton–Schwab algorithm. The sky model generated by the CLEAN components was used to self-calibrate each snapshot over the full bandwidth using a frequency-independent sky model and averaging over the 10-minute observation. We corrected for residual cable length errors by computing antenna-based phase solutions for each frequency channel for each snapshot observation. After self-calibration, snapshot visibilities were again Fourier transformed into images and deconvolved down to a 2 Jy threshold to form the final sky models. These final sky models were used to solve for a frequency-independent, diagonal, complex Jones matrix (Hamaker et al. 1996; Smirnov 2011) for each antenna in order to calibrate gain variations from snapshot to snapshot. We make no attempt to correct sky models for polarized primary beams and therefore our gain solutions incorporate both the direction-independent and the direction-dependent responses of the two gain polarizations. This is a reasonable approximation for the scope of the paper, as eventually wide-field polarization corrections cannot be implemented directly in the per-baseline power spectrum estimation (see Section 3).

The average correction in magnitude through this second-order calibration was a $\pm 6\%$ change for x gains and $\pm 7\%$ for y gains from those derived in the initial delay-space calibration. If the gain on an antenna deviated by more than 30% from image to image during this analysis, it was discarded from future processing stages since it was likely malfunctioning. This was true for three antennae (see the top panel of Figure 1).

The final gain amplitude calibration was carried out similarly to Ali et al. (2015). We generated single channel images between 120 and 174 MHz for each snapshot and deconvolved each of them down to 10 Jy. For each snapshot, a source spectrum is derived for Pictor A by fitting a two-dimensional Gaussian the source using the PyBDSM²¹ source extractor (Mohan & Rafferty 2015). Spectra were optimally averaged together by weighting them with the primary beam model evaluated in the direction of Pictor A. To fit the absolute calibration, we divided the model spectrum (Jacobs et al. 2013) by the measured one and fit a sixth-order polynomial over the 120–174 MHz frequency range. This procedure was repeated using Fornax A with the only difference being that a taper was

¹⁹ <https://github.com/AaronParsons/aipy>

²⁰ <http://casa.nrao.edu>

²¹ <http://www.lofar.org/wiki/doku.php?id=public:usersoftware:pybdsm>

applied to the visibilities (120 m) to reduce Fornax A to a point-like source and use the model spectrum from Bernardi et al. (2013). The best-fit coefficients for Pictor A and Fornax A were averaged together to obtain the final absolute flux density calibration. Snapshots of fully CASA-calibrated data are shown in Figure 2.

2.2.3. Polarimetric Factors

Standard full polarization calibration involves correcting for leakage of Stokes I into the V_{ij}^{xy} and V_{ij}^{yx} visibilities and leakage of polarized signal into total intensity (the so-called Jones D matrices or D -terms; e.g., Thompson et al. 1986; Hamaker et al. 1996), and an unknown phase difference between the x and y feeds (e.g., Sault et al. 1996).

We attempt no D matrix calibration in this paper, as there is not a dominant source to be used for such calibration: the limited sensitivity of our observations does not offer good signal-to-noise ratio on PMN J0351-2744, the only polarized source at low frequencies known so far in our survey area. In addition, D -term calibration would require determination of the primary beam Mueller matrices beyond our current accuracy. (Note that this is an ongoing effort; see Paper II, in preparation). The consequences of this limitation are discussed in the analysis of our power spectra in Section 3.

As a intermediate measure compatible with these limitations, we therefore adopted a minimization of the phase difference between the V_{ij}^{xy} and V_{ij}^{yx} visibilities, minimizing a sum of squared weighted residuals w :

$$w(\nu, t, \tau_{xy}) = \sum_{ij} |V_{ij}^{xy} - V_{ij}^{yx} \exp(-2\pi i \nu \tau_{xy})|^2 \quad (3)$$

to find an estimated value of τ_{xy} for the array at each (ν, t) sample. This is equivalent to assuming that the sky is intrinsically not circularly polarized at the frequencies observed by PAPER.

We choose not to correct for ionospheric Faraday rotation in our calibration. Not only is this difficult to do for widefield instruments, but also the ionosphere was relatively stable during the observations, so we expect little incoherent averaging during the power spectrum stage below. We calculated the stability of ionospheric RM (ϕ_{iono}) using the IONFR software (Sotomayor-Beltran et al. 2013), which calculates the ϕ_{iono} for a given longitude, latitude, and time by interpolating values of GPS-derived total electron content maps and the International Geomagnetic Reference Field (Finlay et al. 2010). The values of ϕ_{iono} for different lines of sight are shown in Figure 3. Fluctuations of ϕ_{iono} will cause incoherent time-averaging and subsequent loss of polarized signal. Using the formalism of Moore et al. (2016) to calculate the attenuation factor, we found that none of the lines of sight (except for the 21 hr, 0° one which goes beneath the horizon) shown are responsible for attenuating signal by $>20\%$ in power-spectrum space (see Section 2.3).

We form linear combinations of the instrument visibilities, the so-called Stokes visibilities (see e.g., Moore et al. 2013) V^I , V^Q , V^U and V^V as

$$\begin{pmatrix} V^I \\ V^Q \\ V^U \\ V^V \end{pmatrix} = \begin{pmatrix} 1 & 0 & 0 & 1 \\ 1 & 0 & 0 & -1 \\ 0 & 1 & 1 & 0 \\ 0 & -i & i & 0 \end{pmatrix} \begin{pmatrix} V^{xx} \\ V^{xy} \\ V^{yx} \\ V^{yy} \end{pmatrix}. \quad (4)$$

Data that were reduced, calibrated, and formed into Stokes visibilities were separated into delay spectra inside and outside of the horizon for each baseline. We used a 50 ns margin for what was considered “inside” the horizon, to confine all supra-horizon emission (e.g., Parsons et al. 2012b; Pober et al. 2013) to the foreground component of the data. We implemented a one-dimensional CLEAN (Parsons & Backer 2009; Parsons et al. 2012a) with a Blackman–Harris window to a tolerance of 10^{-9} . RFI is more easily identified in foreground-removed data, so we RFI-flagged again on the background data deviations greater than 3σ . We then added the inside and outside horizon visibilities back together; RFI flags were preserved in the process.

The effect of our calibration is shown in the delay-transformed visibilities in Figure 4. As is apparent in Figure 2, after improved calibration there are fewer delay tracks (i.e., sources) in the Stokes Q visibilities, while there is little overall change in Stokes U. The minimization of Stokes V, performed after the imaging calibration stage, moves power from Stokes V into Stokes U, effectively accounting for part of a D -term correction. But without an accurate D -term calibrator, Stokes U exhibits additional (and dominant) D -term leakage from Stokes I, in this case due to Pictor A. Pictor A is the brightest source in Stokes I in our observed field, and thus dominates the visibility shown. There is no reason to suppose that Pictor A is pure Stokes U (compare also Figure 2), and thus the bulk of this emission must be leakage.

2.3. Creating Power Spectra

Expressing the visibility $V_{ij}^{pq}(\nu, t)$ observed at time t (see Equation (1)) in terms of the geometrical delay $\tau_g = \mathbf{b}(t) \cdot \hat{\mathbf{s}}(l, m)/c$ for the baseline ij , Parsons et al. (2012b) define the delay transform as the Fourier transform of the visibility along the frequency axis:

$$\tilde{V}_{ij}^{pq}(\tau, t) = \int d\nu V_{ij}^{pq}(\nu, t) e^{2\pi i \nu \tau}. \quad (5)$$

We can represent the power at each frequency and baseline in an array as a power spectrum in terms of their respective Fourier components k_{\parallel} and k_{\perp} as

$$P(k_{\parallel}, k_{\perp}) \approx |\tilde{V}_{ij}^{pq}(\tau, t)|^2 \frac{X^2 Y}{\Omega B} \left(\frac{c^2}{2k_B \nu^2} \right)^2 \quad (6)$$

where B is the bandwidth, Ω is the angular area (i.e., proportional to the beam area), and X and Y are redshift-dependent scalars calculated in Parsons et al. (2012a).

To form $|\tilde{V}_{ij}^{pq}(\tau, t)|^2$, consecutive integrations were cross-multiplied, phasing the zenith of latter to the former, i.e.,

$$|\tilde{V}_{ij}^{pq}(\tau, t)|^2 \approx |V_{ij}^{pq}(\tau, t) \times V_{ij}^{pq}(\tau, t + \Delta t) e^{i\theta_{ij, \text{zen}}(\Delta t)}|^2 \quad (7)$$

where $\Delta t = 10.7$ seconds and $\theta_{ij, \text{zen}}(\Delta t)$ is the appropriate zenith rephasing factor. This method should avoid noise-biased power spectra except on very long baselines, which the PAPER configuration does not contain, while sampling essentially identical k -modes. Note that this is the same method used by Pober et al. (2013) in their investigation of the unpolarized wedge.

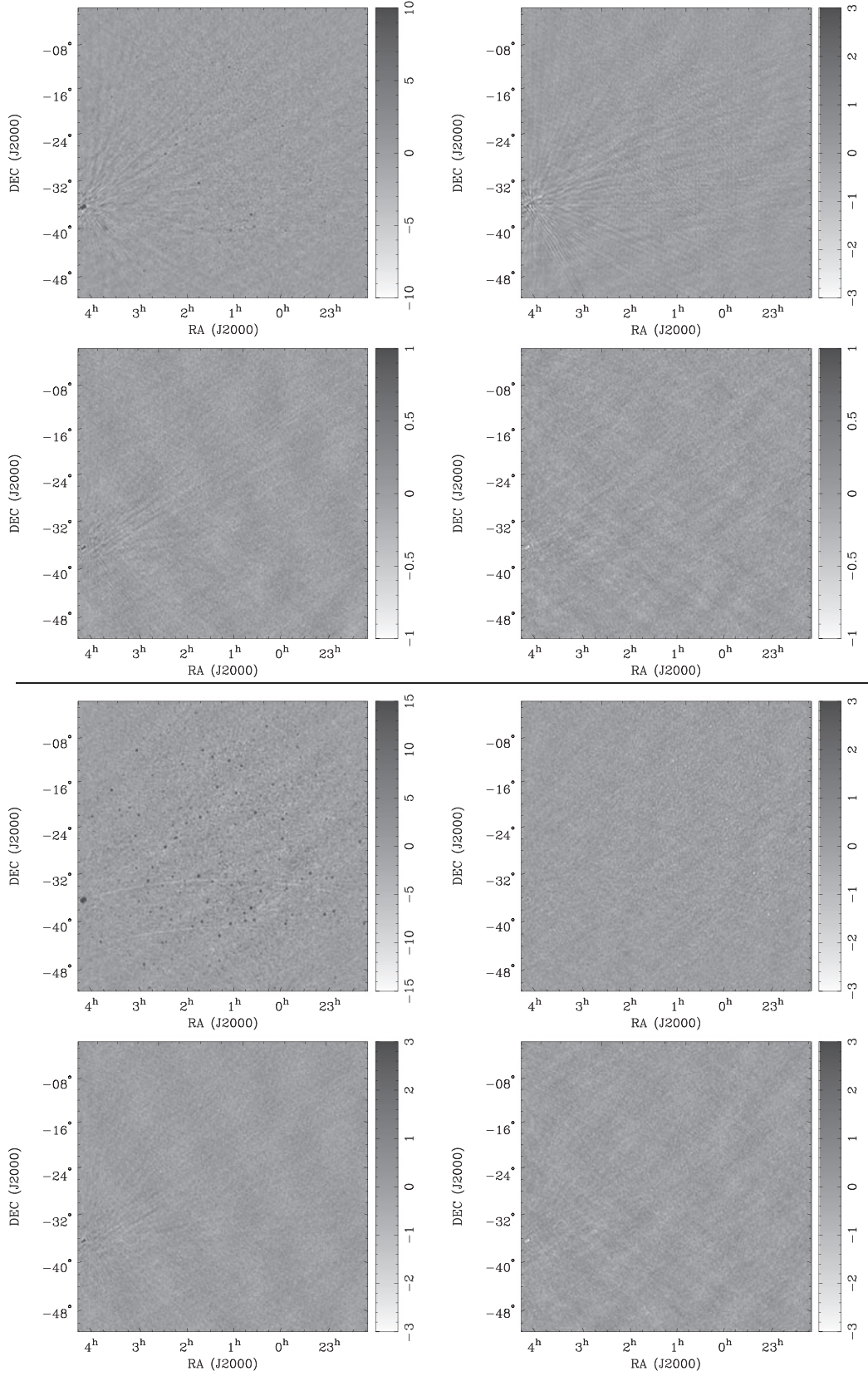


Figure 2. Top four panels: example of a Stokes I snapshot image (top left) with corresponding Stokes Q (top right), Stokes U (bottom left), and Stokes V (bottom right) images before absolute calibration. Bottom four panels: the same organization as the top panels after absolute calibration. No primary beam correction was applied. The Stokes I image was deconvolved down to 5 Jy beam^{-1} , whereas the other images were not deconvolved. We note that the Stokes Q image is relatively featureless apart from a few faint sources that appear instrumentally polarized. Stokes U and Stokes V images are instead dominated by Fornax A, which shows instrumental polarization leaked from total intensity. Units are Jy beam^{-1} ; note the change in scale between polarizations and calibration stages.

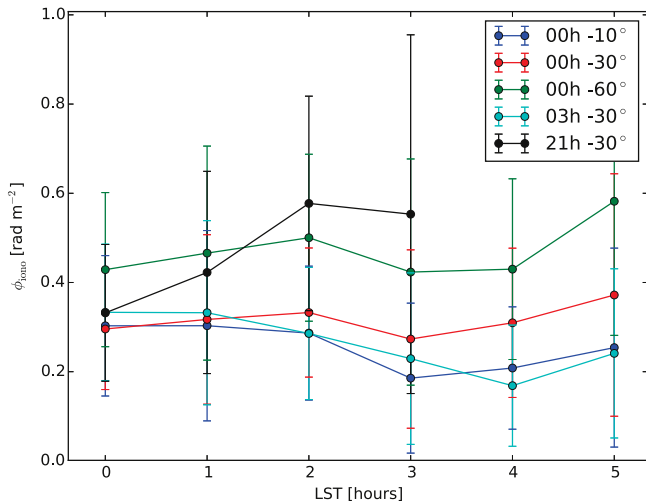


Figure 3. Values of ionospheric RM for different lines of sight for the range of LSTs in this analysis as calculated by `ionFR` (Sotomayor-Beltran et al. 2013). The 21 hr, 0° line of sight goes beneath the horizon after LST = 3 hr, and therefore has fewer data points.

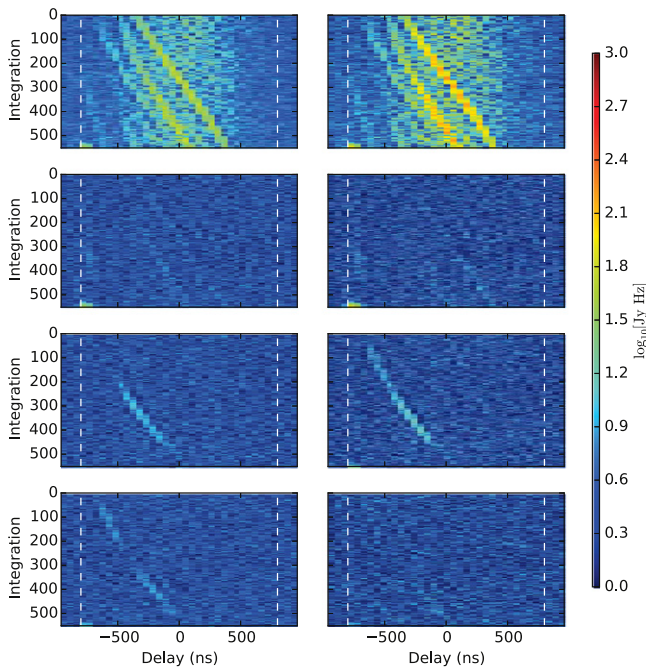


Figure 4. Absolute value of delay-transformed visibilities over the bandwidth (146–166 MHz) used to create the power spectra shown in this work. The left and right columns show the visibilities before and after absolute calibration (and for Stokes U and V, the application of the τ_{xy} parameter), respectively, for the baseline formed by antennae 6 and 14 (~ 250 m in length, approximately east–west). The flux scale in the left column has been boosted for a more fair comparison to the absolute-calibrated data. From top to bottom, the rows correspond to Stokes I, Q, U, and V, respectively. The horizon limit is marked by the white dashed lines.

3. RESULTS

Combining visibilities using Equation (4) we formed power spectra over frequencies 146–166 MHz according to Equation (6), using consecutive integrations for each Stokes visibility over time and gridded our results into k -space, averaging in time. The k_{\perp} -axis is binned with a resolution of $4.65 \times 10^{-4} h \text{ Mpc}^{-1}$ to slightly reduce gaps in k -space due to missing baselines. This gave an average bin occupancy of 1.7 ± 0.9 . The resolution in k_{\parallel} ($5.06 \times 10^{-4} h \text{ Mpc}^{-1}$) is set by the 20 MHz bandwidth with

500 kHz resolution that we use in this analysis. Note that the Blackman–Harris window used in the delay-filtering stage after forming Stokes visibilities correlates adjacent frequency bins, and hence k_{\parallel} bins. Each $(k_{\perp}, k_{\parallel})$ bin was normalized by its occupancy.

Two-dimensional power spectra have proved powerful tools for large dipole array experiments, not only for assessing cosmology but also to constrain instrumental and analytical systematics (e.g., Morales et al. 2012). Polarization axes are a useful addition for such analyses, as we expect Stokes I to be approximately three orders of magnitude stronger than the other polarization products at the low radio frequencies and tens-of-arcminute scales native to PAPER observations (e.g., Pen et al. 2009; Moore et al. 2013) and when observing far from the Galactic Plane. This alone allows us to assume that much of the structure in the power spectra with power comparable to Stokes I is leakage. As we explore below, these leakage terms can come from direction-dependent effects (e.g., wide-field beam leakage; Carozzi & Woan 2009) or direction-independent ones (e.g., Mueller matrix mixing via gain errors and D-terms; Thompson et al. 1986) and appear with high signal-to-noise in power spectra.

Figure 5 shows power spectra in “pitchfork” form (Thyagarajan et al. 2015b, 2015a), with k_{\parallel} in negative and positive directions (according to the East and West horizons, marked in white (horizon) and orange (horizon+50 ns delay, respectively). Each Stokes parameter pitchfork has its own interesting characteristics, which allow us to analyze different sky and instrument behaviors. The “wedges” described in the literature that define the EoR window are simply the average of negative and positive values of k_{\parallel} . While we focus on the pitchfork expression of the power spectra in our results, we also show them in wedge²² form in Figure 6.

Simplifying the results of Thyagarajan et al. (2015b, 2015a, see their papers for a full discussion), we expect power from diffuse emission to appear at low values of k_{\perp} and high values of k_{\parallel} , while point sources lie at all k_{\parallel} (all over the sky) but are down-weighted by the primary beam, which is broad, leaving a concentration of the power close to the $k_{\parallel} = 0$ line.

In Stokes I, we see the strongest power on most baselines arising at values $k_{\parallel} \approx 0$. This is expected in a situation of point sources that are relatively bright compared to any diffuse emission. Indeed, at the LSTs we observed at, several unresolved bright point sources transit the field (e.g., Figure 2), while the dominant source of diffuse emission at these frequencies, the Galactic plane, was below the horizon. However, we do see strong super-horizon emission at $0.02 \leq k_{\perp} \leq 0.03$, biased toward negative k_{\parallel} values. There is also a decrease in power with increasing k_{\perp} —both of these effects are consistent with the Thyagarajan et al. (2015a) simulations of faint diffuse structure transiting zenith.

The Stokes Q wedge shows a concentration of power close to $k_{\parallel} \approx 0$, similar to Stokes I. The inherent low polarization fraction at our frequencies works in our favor in detecting gain errors, since Stokes Q is largely expected to be faint, and thus the gain errors causing leakage from I appear at high signal-to-noise there. Indeed, this power decreases noticeably with more accurate gain amplitude calibration, but bright streaks at

²² Note the difference in the power distribution within the horizon differs from that shown in the Pober et al. (2013) V^{xy} wedge. That study used the PAPER 64-element, single-polarization imaging array to create power spectra in a “loud” field containing point sources and Galactic signal, causing their wedge to be “fuller” than the ones presented in this study.

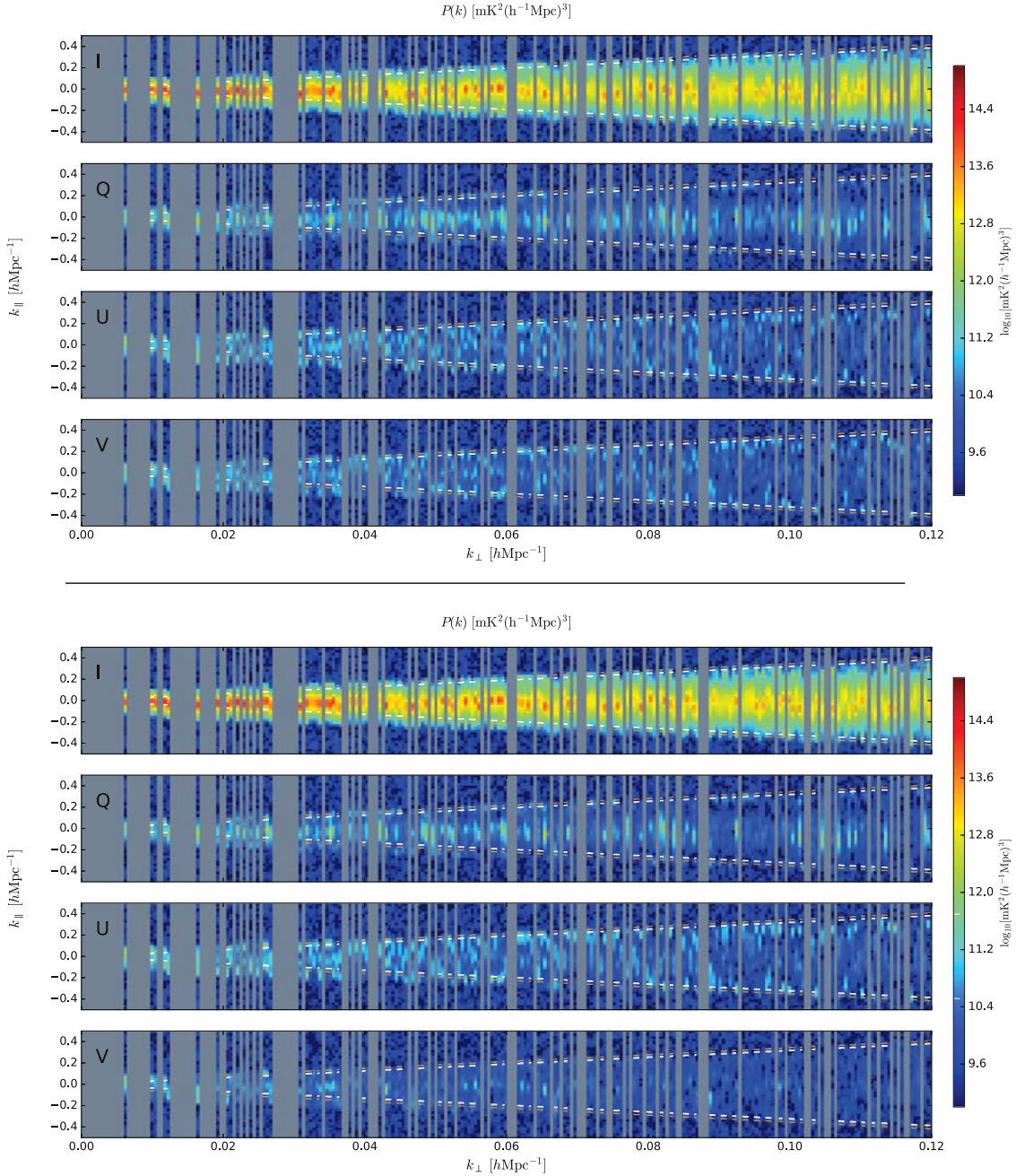


Figure 5. Top panel: log-scaled 2D power spectra formed from (top to bottom): I, Q, U, and V visibilities after before absolute calibration. Blank regions indicate the incomplete uv coverage for a given k_{\perp} (u). The color bar spans 10^9 to 10^{15} $\text{mK}^2(h^{-1}\text{Mpc})^3$. The flux scale has been boosted for a more fair comparison to the absolute-calibrated data. Bottom panel: the same organization as above, but after absolute calibration. Briefly, the structure in Stokes I is consistent with a point-source-dominated field with a weak diffuse component. The other Stokes parameters are consistent with calibration errors and systematics: Stokes Q shows gain errors on specific antennae, Stokes U gives an estimate of possible D-term leakage, and any structure in V shows unaccounted for systematics due to D-terms or mis-oriented antennae.

specific values of k_{\perp} remain, suggesting lower-level residual gain calibration errors on select baselines. Another possible source of power in Stokes Q stems from widefield direction-dependent gain errors causing a non-smooth evolution of the sources on the edges of the beam. However, we would expect this effect to be biased toward horizon values of k_{\parallel} .

Power appears distributed in “pockets” in the Stokes U power spectrum, not strongly correlated with the distribution of power in I. Stokes I is able to leak into Stokes U via D -term leakage (Thompson et al. 1986; Geil et al. 2011), which could occur at any post-amplification stage of observations, such as in cables or receivers. These leakages would be direction

independent, and therefore uncorrelated in k -space. Such a mechanism could explain the behavior within Stokes U wedge. Before absolute calibration, similar structure is seen in the Stokes V power spectrum.

At these frequencies, Stokes V is thought to be intrinsically zero, with few exceptions. However, Hamaker et al. (1996) show that antennae rotated with respect to one another can produce erroneous Stokes V power via $I \rightarrow V$ leakage.²³ This

²³ It should be noted that while such an error could plausibly have been made in the antenna placement for this imaging array, it is extremely unlikely that it would be made in the redundant PAPER configuration for EoR seasons. In these cases, the antennae were positioned to sub-cm accuracy.

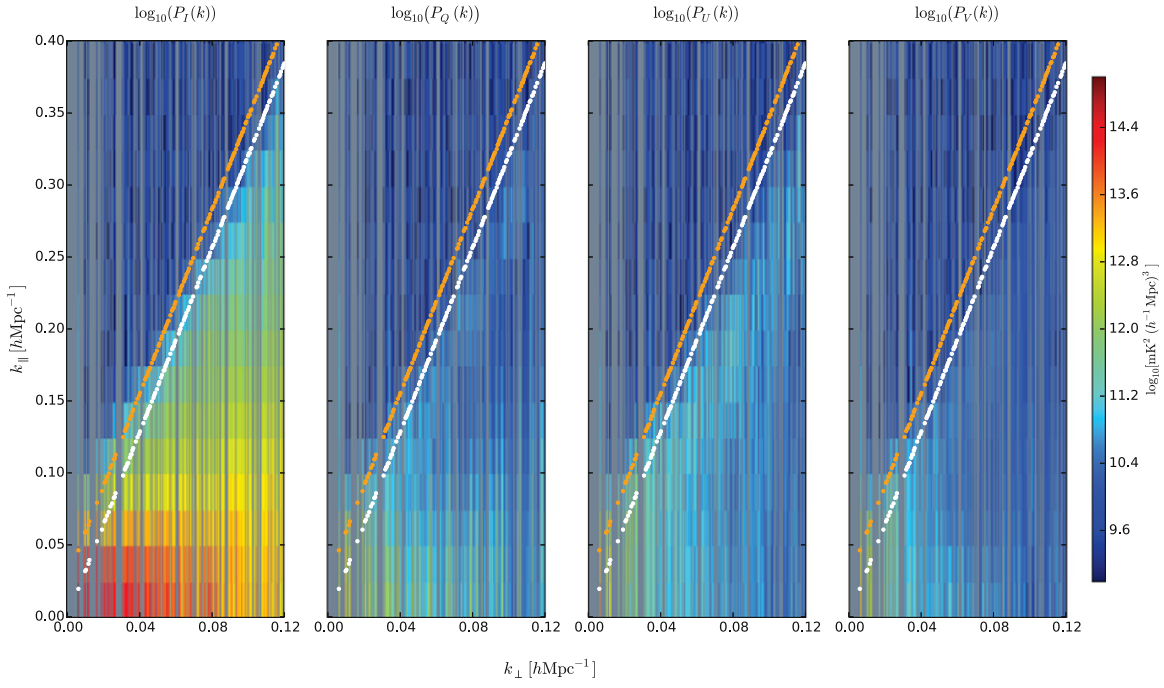


Figure 6. Log-scaled 2D power spectra formed from (left to right): I, Q, U, and V absolute-calibrated visibilities. Blank regions indicate the incomplete uv coverage for a given $k_{\perp}(u)$. The white and orange lines indicate the horizon and horizon plus a 50 ns boundary for super-horizon emission.

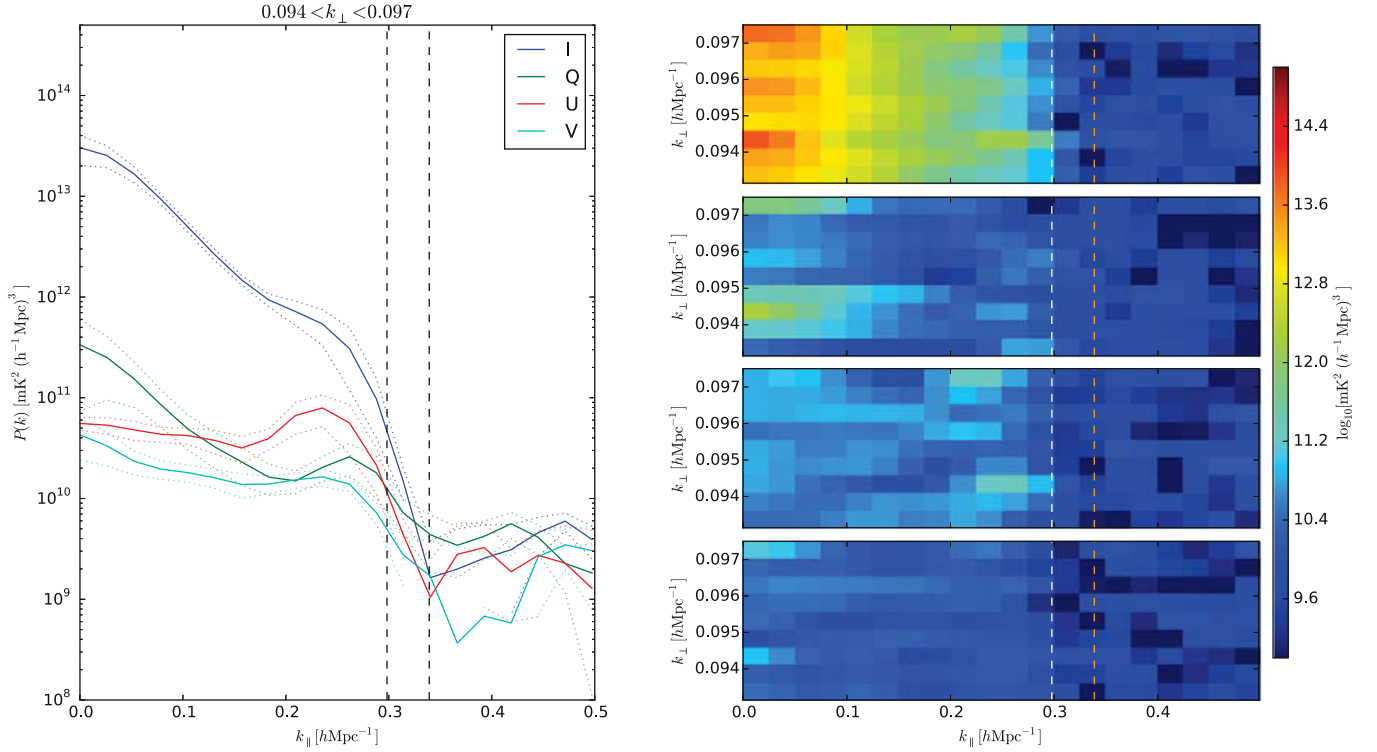


Figure 7. Left: the average power in $0.093 < k_{\perp} < 0.098 \text{ hMpc}^{-1}$ as a function of k_{\parallel} for each polarization. In the horizon–super-horizon range that we see the sharp fall-off in power indicative of the edge of the EoR window. Outside of the wedge, Stokes I, Q and U are at noise level, while Stokes V is below noise level, most likely due to the τ_{xy} calibration scheme removing a degree of freedom from this Stokes parameter. Right: the region of k -space that was averaged over to create the lines in the left panel. From top to bottom, the panels correspond to Stokes I, Q, U and V.

effect may explain some of the small pockets of power that remain in the Stokes V power spectrum after absolute calibration, although such an effect is also consistent with D -term leakage. The fact that power within the horizon is greater than the noise level may also be due to $I \rightarrow V$ leakage through the primary beam.

The relationship between polarizations is highlighted in Figure 7. We show a slice of the wedges over $0.097 < k_{\perp} < 0.098 \text{ hMpc}^{-1}$ ($\sim 175 \text{ m}$) for Stokes I, Q, U and V (right panels) and the average power over these slices as a function of k_{\parallel} (left panel). The standard deviations for each Stokes parameter are shown as dotted lines. Dashed vertical

lines show the horizon at $k_{\perp} = 0.097$ (left) and super-horizon at $k_{\perp} = 0.098$ (right).

A heartening aspect of Figure 7, and indeed all of the power spectra in this work, is that the power in Stokes Q, U, and V proves to be just as confined within the horizon as Stokes I. Whether the polarized Stokes parameters are due to real polarization or miscalibration, not enough spectral structure is being introduced to move emission into the EoR window. Outside of the horizon, Stokes I, Q, and U are consistent with the noise level expected for this range of k -modes ($P_{\text{noise}} \sim 10^9 \text{ mK}^2 (h^{-1} \text{Mpc})^3$), according to the formalism of Parsons et al. (2012a) and assuming a system temperature $T_{\text{sys}} = 450 \text{ K}$ (e.g., Moore et al. 2016).

4. DISCUSSION AND CONCLUSIONS

We presented measurements of instrumental polarization leakage in PAPER-32 using 2D power spectra. These allowed us to quantify some of the possible instrumental effects that could limit a statistical detection of the EoR within the wedge, diagnosed in the Fourier space most relevant EoR statistical detection experiments. To our knowledge, this is the first study of Q, U, and V 2D power spectra at these k -modes. We showed that power from Stokes Q, U, and V is as confined to the wedge as Stokes I. Any calibration errors do not appear to spread power outside the horizon.

In their study of 2D power spectra, Asad et al. (2015) reported evidence of polarized leakage into the EoR window at the sub-percent level, considering a 4° degree field of view. Their study differs from this work not only over the field of view (4° versus almost whole-sky), but also in the observing mode (tracked versus drift scan) and in the different k -space probes by LOFAR’s longer baselines. In this work, the power spectrum is calculated on a per-baseline basis, whereas their study calculates power spectra for gridded data which are more prone to mode mixing effects (Hazelton et al. 2013).

Our results are expected in principle to be more prone to leakage contamination due to the intrinsic extremely wide field of view of the PAPER primary beams; however, we see no evidence of leakage in the EoR window down to our sensitivity limits even without the correction for polarized beams that is instead included in Asad et al. (2015). Our analysis indicates, therefore, that neither intrinsic polarized emission nor the PAPER primary beam are leaking power in the EoR window, although longer integrations are required to demonstrate that this is true down to the sensitivities required for EoR detection.

We showed that systematics can be probed with high signal-to-noise using 2D polarized power spectra, using the inherently low polarization fraction at the frequencies PAPER observes at to our advantage. We found that gain errors on specific baselines were easily probed using Stokes Q power spectra. Gain errors appear as continuous streaks within the horizon at specific values of k_{\perp} , allowing us to diagnose the precision of the gain calibration on a per-baseline basis. This is much more difficult to do with only Stokes I power spectra in a non-redundant array and can be accomplished quickly without imaging. While the features in the Stokes U power spectra are more difficult to attribute to specific baselines, they appear to be consistent with direction-independent leakage. Stokes V power is slightly higher than noise level within the horizon, suggesting a small but unaccounted for leakage term from Stokes I, an effect which will be explored in Paper II.

The measurements presented here came from PAPER 32-antenna data taken in 2011. PAPER has since placed limits on the EoR power spectrum using redundant-array 32-element (e.g., Parsons et al. 2014) and 64-element data (e.g., Ali et al. 2015). Moore et al. (2016) showed limits on the polarized power spectrum with 32-element data. Limits on the polarized power spectrum from PAPER-64 and PAPER-128 are currently being worked on, which will allow us to more fully quantify the effect of polarized foregrounds on a statistical detection of the EoR. The PAPER-64 array was a purely redundant grid, but PAPER-128 contains outrigger antennae that provide greater uv coverage than the data we present in this work. A future paper will show power spectra from this array, which can leverage OMNICAL’s precise redundant calibration for most of the antennae and more than 1000 hr of integration time to produce extremely deep measurements of polarization.

The authors thank Adam Beardsley, Bryna Hazelton, Zachary Martinot, Miguel Morales, and Nithyanandan Thyagarajan for helpful conversations, and the anonymous referee for the helpful comments.

We thank SKA SA for their efforts in ensuring the smooth running of PAPER. PAPER is supported through the NSF AST program (awards 0804508, 1129258, and 1125558), the Mount Cuba Astronomical Association, and by significant efforts by the staff at NRAO. This work is based on research supported by the National Research Foundation under grant 92725. Any opinion, finding, and conclusion or recommendation expressed in this material is that of the author(s) and the NRF does not accept any liability in this regard. The financial assistance of the South African SKA Project (SKA SA) toward this research is hereby acknowledged. Opinions expressed and conclusions arrived at are those of the authors and are not necessarily to be attributed to the SKA SA. C.D.N. is supported by the SKA SA scholarship program. A.R.P. acknowledges support from the University of California Office of the President Multicampus Research Programs and Initiatives through award MR-15-328388, as well as from NSF CAREER award No. 1352519, NSF AST grant No. 1129258, and NSF AST grant No. 1440343.

REFERENCES

- Ali, Z. S., Parsons, A. R., Zheng, H., et al. 2015, *ApJ*, 809, 61
- Asad, K. M. B., Koopmans, L. V. E., Jelić, V., et al. 2015, *MNRAS*, 451, 3709
- Bernardi, G., de Bruyn, A. G., Brentjens, et al. 2009, *A&A*, 500, 965
- Bernardi, G., de Bruyn, A. G., Harker, G., et al. 2010, *A&A*, 522, A67
- Bernardi, G., Greenhill, L. J., Mitchell, D. A., et al. 2013, *ApJ*, 771, 105
- Carozzi, T. D., & Woan, G. 2009, *MNRAS*, 395, 1558
- Chapman, E., Zaroubi, S., Abdalla, F., et al. 2016, *MNRAS*, 458, 2928
- Datta, A., Bowman, J. D., & Carilli, C. L. 2010, *ApJ*, 724, 526
- Dillon, J. S., Liu, A., Williams, C. L., et al. 2014, *PhRvD*, 89, 023002
- Dillon, J. S., Tegmark, M., Liu, A., et al. 2015a, *PhRvD*, 91, 123011
- Dillon, J. S., Neben, A. R., Hewitt, J. N., et al. 2015b, *PhRvD*, 91, 023002
- Ewall-Wice, A., Bradley, R., DeBoer, D., et al. 2016, arXiv:1602.06277
- Farnes, J. S., Gaensler, B. M., & Carretti, E. 2014, *ApJS*, 212, 15
- Finlay, C. C., Maus, S., Beggan, C. D., et al. 2013, *GeoJI*, 183, 1216
- Furlanetto, S. R., Oh, S. P., & Briggs, F. H. 2006, *PhR*, 433, 181
- Geil, P. M., Gaensler, B. M., & Wyithe, J. S. B. 2011, *MNRAS*, 418, 516
- Hamaker, J. P., Bregman, J. D., & Sault, R. J. 1996, *A&AS*, 117, 137
- Hazelton, B. J., Morales, M. F., & Sullivan, I. S. 2013, *ApJ*, 770, 156
- Jacobs, D. C., Parsons, A. R., Aguirre, J. E., et al. 2013, *ApJ*, 776, 108
- Jacobs, D. C., Pober, J. C., Parsons, A. R., et al. 2015, *ApJ*, 801, 51
- Jelić, V., Zaroubi, S., Labropoulos, P., et al. 2010, *MNRAS*, 409, 1647
- Jelić, V., de Bruyn, A. G., Mevius, M., et al. 2014, *A&A*, 568, A101
- Jelić, V., de Bruyn, A. G., Pandey, V. N., et al. 2015, *A&A*, 583, A137

- Lidz, A., Zahn, O., McQuinn, M., Zaldarriaga, M., & Hernquist, L. 2008, *ApJ*, **680**, 962
- Liu, A., Parsons, A. R., & Trott, C. M. 2014a, *PhRvD*, **90**, 023018
- Liu, A., Parsons, A. R., & Trott, C. M. 2014b, *PhRvD*, **90**, 023019
- Mohan, N., & Rafferty, D. 2015, PyBDSM: Python Blob Detection and Source Measurement, Astrophysics Source Code Library, ascl:1502.007
- Moore, D. F., Aguirre, J. E., Parsons, A. R., Jacobs, D. C., & Pober, J. C. 2013, *ApJ*, **769**, 154
- Moore, D., Aguirre, J. E., Kohn, S. A., et al. 2016, arXiv:1502.05072
- Morales, M. F., Hazelton, B., Sullivan, I., & Beardsley, A. 2012, *ApJ*, **752**, 137
- Neben, A. R., Bradley, R. F., Hewitt, J. N., et al. 2016, arXiv:1602.03887
- Paciga, G., Chang, T.-C., Gupta, Y., et al. 2011, *MNRAS*, **413**, 1174
- Parsons, A., Pober, J., McQuinn, M., Jacobs, D., & Aguirre, J. 2012a, *ApJ*, **753**, 81
- Parsons, A. R., & Backer, D. C. 2009, *AJ*, **138**, 219
- Parsons, A. R., Pober, J. C., Aguirre, J. E., et al. 2012b, *ApJ*, **756**, 165
- Parsons, A. R., Backer, D. C., Foster, G. S., et al. 2010, *AJ*, **139**, 1468
- Parsons, A. R., Liu, A., Aguirre, J. E., et al. 2014, *ApJ*, **788**, 106
- Pen, U.-L., Chang, T.-C., Hirata, C. M., et al. 2009, *MNRAS*, **399**, 181
- Pober, J. C., Ali, Z. S., Parsons, A. R., et al. 2014, *ApJ*, **782**, 66
- Pober, J. C., Liu, A., Dillon, J. S., et al. 2013, *ApJL*, **768**, L36
- Sault, R. J., Hamaker, J. P., & Bregman, J. D. 1996, *A&AS*, **117**, 149
- Smirnov, O. M. 2011, *A&A*, **527**, A106
- Sotomayor-Beltran, C., Sobey, C., Hessels, J. W. T., et al. 2013, *A&A*, **552**, A58
- Thompson, A. R., Moran, J. M., & Swenson, G. W. 1986, *Interferometry and Synthesis in Radio Astronomy* (New York: Wiley-Interscience)
- Thyagarajan, N., Jacobs, D. C., Bowman, J. D., et al. 2015a, *ApJ*, **804**, 14
- Thyagarajan, N., Jacobs, D. C., Bowman, J. D., et al. 2015b, *ApJL*, **807**, L28
- Thyagarajan, N., Udaya Shankar, N., Subrahmanyam, R., et al. 2013, *ApJ*, **776**, 6
- Tingay, S. J., Goeke, R., Bowman, J. D., et al. 2013, *PASA*, **30**, 7
- Trott, C. M., Wayth, R. B., & Tingay, S. J. 2012, *ApJ*, **757**, 101
- van Haarlem, M. P., Wise, M. W., Gunst, A. W., et al. 2013, *A&A*, **556**, A2